

**Strong topological metal material with multiple Dirac cones**Huiwen Ji,<sup>1</sup> I. Pletikosić,<sup>2,3</sup> Q. D. Gibson,<sup>1</sup> Girija Sahasrabudhe,<sup>1</sup> T. Valla,<sup>3</sup> and R. J. Cava<sup>1</sup><sup>1</sup>*Department of Chemistry, Princeton University, Princeton, New Jersey 08544, USA*<sup>2</sup>*Department of Physics, Princeton University, Princeton, New Jersey 08544, USA*<sup>3</sup>*Condensed Matter Physics and Materials Science Department, Brookhaven National Laboratory, Upton, New York 11973, USA*

(Received 1 December 2015; published 25 January 2016)

We report a new, cleavable, strong topological metal,  $\text{Zr}_2\text{Te}_2\text{P}$ , which has the same tetradymite-type crystal structure as the topological insulator  $\text{Bi}_2\text{Te}_2\text{Se}$ . Instead of being a semiconductor, however,  $\text{Zr}_2\text{Te}_2\text{P}$  is metallic with a pseudogap between 0.2 and 0.7 eV above the Fermi energy ( $E_F$ ). Inside this pseudogap, two Dirac dispersions are predicted: one is a surface-originated Dirac cone protected by time-reversal symmetry (TRS), while the other is a bulk-originated and slightly gapped Dirac cone with a largely linear dispersion over a 2 eV energy range. A third surface TRS-protected Dirac cone is predicted, and observed using angle-resolved photoemission spectroscopy, making  $\text{Zr}_2\text{Te}_2\text{P}$  the first system, to our knowledge, to realize TRS-protected Dirac cones at  $\bar{M}$  points. The high anisotropy of this Dirac cone is similar to the one in the hypothetical Dirac semimetal  $\text{BiO}_2$ . We propose that if  $E_F$  can be tuned into the pseudogap where the Dirac dispersions exist, it may be possible to observe ultrahigh carrier mobility and large magnetoresistance in this material.

DOI: [10.1103/PhysRevB.93.045315](https://doi.org/10.1103/PhysRevB.93.045315)**I. INTRODUCTION**

Three-dimensional (3D) Dirac materials that host massless Dirac fermions have recently received widespread attention due to their exotic properties such as extremely high carrier mobility and large magnetoresistance [1–3]. They are the 3D analogs of graphene, with Dirac points and “photonlike” dispersions in their electronic structures. The Dirac bands can have different origins. Breaking their protecting symmetries causes the Dirac point to be gapped and leads to a Dirac band where the electrons have mass. Topological insulators such as  $\text{Bi}_2\text{Te}_3$  and  $\text{Bi}_2\text{Se}_3$  have a finite bulk band gap due to spin-orbit coupling (SOC) and chiral, massless Dirac surface states [4,5]. In these materials, the degeneracy at the surface Dirac point is protected by time-reversal symmetry (TRS) [6,7]. The Dirac points are doubly degenerate and the corresponding surface states are strongly spin polarized. By contrast, another group of 3D Dirac materials—Dirac semimetals—have Dirac dispersions in the bulk electronic structure with Dirac points that are protected by crystalline symmetries [8]. Their Dirac points are fourfold degenerate and do not have spin polarization. Recently established Dirac semimetals include  $\text{Cd}_3\text{As}_2$  [2,9,10] and  $\text{Na}_3\text{Bi}$  [3,11].

Given the potential applications and intrinsically unusual physics of 3D Dirac materials, new candidates are wanted to diversify the current family. Among different material systems, layered chalcogenides containing heavy elements are favored for having the band degeneracies necessary for either 3D Dirac dispersions or topologically protected surface states. Their layered structures and easy cleavage allow visualization of any Dirac dispersion that may be present through angle-resolved photoemission spectroscopy (ARPES) study. The tetradymite structure type is of particular importance as it hosts many 3D topological insulators, namely,  $\text{Bi}_2\text{Te}_3$ ,  $\text{Bi}_2\text{Se}_3$ ,  $\text{Sb}_2\text{Te}_3$ ,  $\text{Bi}_2\text{Te}_2\text{Se}$ , and  $\text{Bi}_2\text{Te}_{1.6}\text{S}_{1.4}$  [5,12,13]. These materials all have a single 2D surface Dirac cone in the Brillouin zone. Here, we report an additional strong topological metal,  $\text{Zr}_2\text{Te}_2\text{P}$ , in the tetradymite structure family. Its multiple Dirac features, which originate from both the bulk and the surface, are

theoretically predicted and experimentally observed using ARPES. In contrast with the majority of currently known topological materials, which are based on  $s$ - $p$  band inversions, the band inversions in  $\text{Zr}_2\text{Te}_2\text{P}$  are of the  $d$ - $p$  type.

**II. EXPERIMENT**

In this work, single crystals of both pristine  $\text{Zr}_2\text{Te}_2\text{P}$  and slightly Cu-intercalated  $\text{Cu}_{0.06}\text{Zr}_2\text{Te}_2\text{P}$  were grown through vapor transport [14]. Initially, adding copper was intended to increase the  $E_F$  of pristine  $\text{Zr}_2\text{Te}_2\text{P}$  because copper intercalation in layered chalcogenides has been known to inject electrons while maintaining the overall band structure [15,16]. We could intercalate only 0.06 Cu per formula unit, (determined using single-crystal x-ray diffraction; see Table I in the Supplemental Material [17]), i.e., 0.03 electrons per Zr, which can raise  $E_F$  only minimally in this metallic material. We found, however, that the as-grown Cu intercalated crystals have higher quality, and therefore the experimental characterizations were performed on  $\text{Cu}_{0.06}\text{Zr}_2\text{Te}_2\text{P}$ , which we designate as  $\text{Cu-Zr}_2\text{Te}_2\text{P}$  in the following.

The sample synthesis followed the methods reported elsewhere [14]. Polycrystalline samples of  $\text{Zr}_2\text{Te}_2\text{P}$  and  $\text{Cu-Zr}_2\text{Te}_2\text{P}$  were made through traditional solid state synthesis at 1000°C. The starting formulas were  $\text{Zr}_2\text{Te}_2\text{P}$  and  $\text{Cu}_{0.8}\text{Zr}_2\text{Te}_2\text{P}$ , respectively. Careful control of the temperature and close monitoring were required to avoid explosion due to phosphorus’s high vapor pressure and the large enthalpy of formation of the product. The polycrystalline powder was then loaded into a quartz ampoule containing iodine as a transport agent. A temperature gradient for chemical vapor transport was created by using a horizontal two-zone furnace with the source end set at 800°C and the sink end at 900°C for five days. Scattered silvery hexagonal platelets formed at the hot end. The layered crystal structure of  $\text{Cu}_{0.06}\text{Zr}_2\text{Te}_2\text{P}$  was confirmed by using powder x-ray diffraction. Single crystals of  $\text{Cu}_{0.06}\text{Zr}_2\text{Te}_2\text{P}$  were selected and studied by using a Photon 100 single-crystal x-ray diffractometer with a Mo radiation source.

The ARPES maps over a two-dimensional momentum space were acquired at the HERS end station of the Advanced Light Source (Berkeley, CA) by rotating the Scienta R4000 electron analyzer around the axis parallel to the direction of its entrance aperture. Photons of 50 eV were used as the excitation. The resolution was set to 25 meV in energy, and  $0.2^\circ$  and  $0.5^\circ$  in the angles. The samples were cleaved and kept at 15 K in ultrahigh vacuum in the course of the measurements.

The electronic structure calculations were performed in the framework of density functional theory (DFT) using the WIEN2K code with a full-potential linearized augmented plane-wave and local orbitals basis [18–20] together with the Perdew-Burke-Ernzerhof parametrization of the generalized gradient approximation as the exchange-correlation functional. The plane-wave cutoff parameter  $R_{\text{MT}}K_{\text{max}}$  was set to 7, and the reducible Brillouin zone was sampled by 2000  $k$  points. The lattice parameters and atomic positions employed for the structural input are from Ref. [14]. For the slab calculation for surface electronic structure simulation, a  $10 \times 10 \times 1$   $k$  mesh was used.

### III. RESULTS AND DISCUSSION

As shown in Fig. 1(a),  $\text{Zr}_2\text{Te}_2\text{P}$  crystallizes in the same structure as the well-known topological insulator  $\text{Bi}_2\text{Te}_2\text{Se}$  [21], with a rhombohedral space group  $R\bar{3}m$  (no. 166). Each unit cell is composed of three quintuple atomic layers, which are separated from each other by van der Waals gaps. In both crystal structures, the more electropositive element (Zr or Bi) takes the  $6c$  Wyckoff position and adopts octahedral coordination. Like  $\text{Bi}_2\text{Te}_2\text{Se}$ ,  $\text{Zr}_2\text{Te}_2\text{P}$  has a fully ordered crystal structure with distinct Wyckoff positions for P and Te (see Table I in the Supplemental Material [17]). A typical scanning electron microscopy (SEM) image of a single crystal piece is shown in Fig. 1(c). The crystal surface was exfoliated with Scotch tape before imaging, exposing a microscopically smooth face under SEM. Its  $120^\circ$  edges are a reflection of the hexagonal close packing of atoms within the layers. The Miller index (001) of the basal plane crystal surface is confirmed by an x-ray diffraction pattern taken on a piece of single crystal [Fig. 1(b)], where only (003 $n$ ) reflections are visible.

The calculated bulk electronic structure of  $\text{Zr}_2\text{Te}_2\text{P}$ , with spin-orbit coupling included, is shown in Fig. 2; the metallic features agree well with previous transport measurements on this compound [14]. The three most important bands near  $E_F$  are denoted by black arrows and the labels Band 1, 2, and 3. The band dispersions are plotted along four time-reversal-invariant momenta (TRIMs). Several flatly dispersive bands observed along the  $\Gamma - Z$  direction originate from the poor orbital overlap along the  $c$  axis of the structurally two-dimensional compound. Nevertheless, there remain some steep dispersions along the  $\Gamma - Z$  direction due to the hybridization of Zr  $4d_{z^2}$  orbitals and Te  $5p_z$  orbitals. We observe a pseudogap between the energies of 0.2 and 0.7 eV above  $E_F$  at the  $\Gamma$  point (between Band 1 and Band 2), which agrees closely with a strong suppression of the density of states (DOS) in the calculation (Fig. S2 in the Supplemental Material [17]). In addition, a rather flat band is observed at around  $-3.25$  eV below  $E_F$ , which mostly comes from P  $3p$  orbitals. As expected, sharp peaks in the DOS from P are observed in the DOS calculation (Fig. S2). Because of

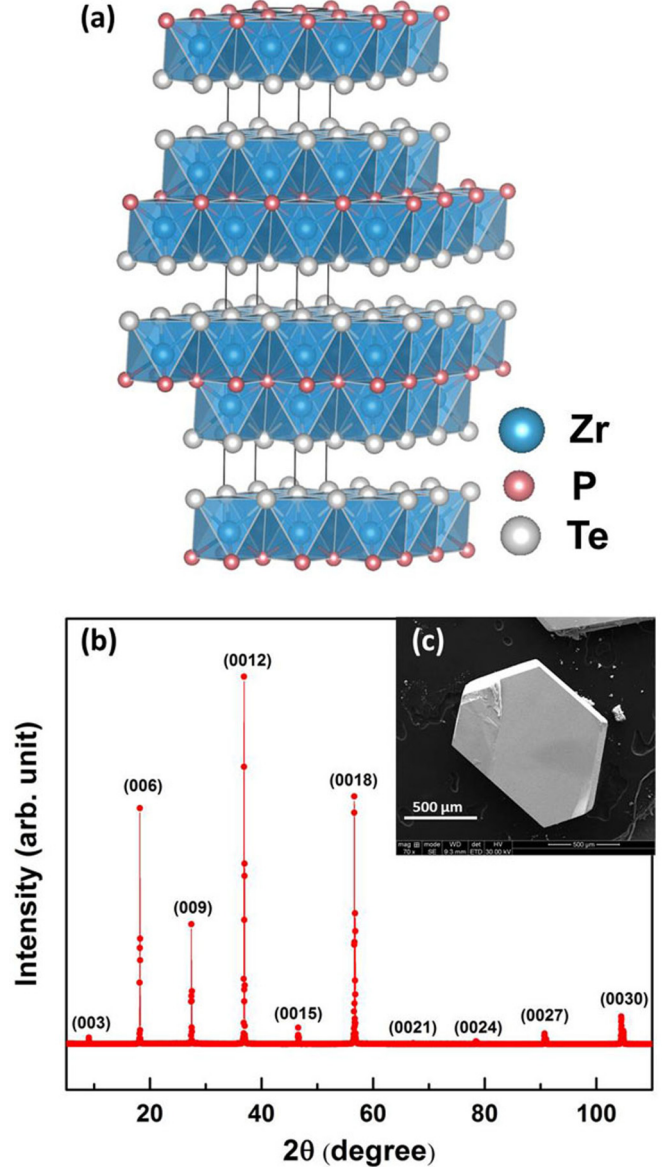


FIG. 1. (a) The crystal structure of  $\text{Zr}_2\text{Te}_2\text{P}$ . (b) X-ray diffraction pattern from the basal plane crystal surface of  $\text{Cu-Zr}_2\text{Te}_2\text{P}$ . (c) SEM image of a typical  $\text{Cu-Zr}_2\text{Te}_2\text{P}$  single crystal.

the large electronegativity difference between Zr and P, the bonded electrons are localized with low mobility.

When SOC is included in the DFT calculations, a band inversion is predicted at the  $\Gamma$  point [highlighted by a red circle in Fig. 2(a)]. This band inversion happens between the Zr  $4d$  orbitals and the Te  $5p$  orbitals. The band dispersions in Figs. 2(b) and 2(c) are Zr  $4d$  orbital and Te  $5p$  orbital characteristic plots, respectively. As shown, the Zr  $4d$  orbital dominates the entire conduction band above the pseudogap while vanishing at the tip; the Te  $5p$  orbital acts oppositely. These observations imply a band inversion between the two orbitals. The surface states that originate due to this band inversion (a Dirac cone) are topologically nontrivial according to the parity analysis of the topmost isolated bands below Band 1 (bands buried deeper are ignored as they do not alter



whose size is proportional to the contribution from the surface atomic layer. A linear dispersion of surface states is observed inside the pseudogap with the band degeneracy/surface Dirac point (SDP, highlighted by a red circle) occurring at around 0.4 eV above  $E_F$ . Unfortunately, these calculated surface states are difficult to visualize through ARPES as they are above  $E_F$ , and only occupied states are visible by that technique. Integration of the DOS suggests that 0.6–0.8 electrons per formula unit are needed to dope the system into the pseudogap.

Nevertheless, in the slab calculations, a third Dirac-cone-like feature is found at the  $\bar{M}$  point at around  $-0.8$  eV below  $E_F$  [highlighted by a green circle in Fig. 3(a)]. It has linear dispersions around it in a 0.4 eV energy window. This cone was absent in the bulk electronic structure calculation, and thus originates from the surface. Meanwhile, the fact that the cone is located at the  $\bar{M}$  point, on the edge of the first surface Brillouin zone, indicates that there are three such cones in the first surface Brillouin zone. The two bands are degenerate at the time-reversal-invariant  $\bar{M}$  while the degeneracy is lifted away from  $\bar{M}$ . This Dirac cone is highly anisotropic, similar to the Dirac cone predicted for the hypothetical topological Dirac semimetal BiO<sub>2</sub> [8]. It has photonlike massless dispersions along  $\bar{M} \rightarrow \bar{K}$  but is almost flat along  $\bar{\Gamma} \rightarrow \bar{M}$  (meaning the electron velocity is almost zero). Notice that the two Dirac bands along  $\bar{M} \rightarrow \bar{\Gamma}$  are so close to each other that they almost form a Dirac line.

Recently it has been shown that even strong topological insulators with a nontrivial parity invariant can have gapped surface states if away from TRIM points [23]. Although  $\bar{M}$  is a time-reversal-invariant point,  $\bar{K}$  is not. Therefore, to analyze the topological nature of this Dirac cone, a parity analysis similar to that performed for the Dirac cone at  $\Gamma$  was performed regarding the gap between Band 2 and Band 3 [Fig. 2(a)]. The  $Z_2$  topological quantum number  $\nu_0$  was again calculated to be 1 (positive parity at  $\Gamma$ ,  $Z$ , and  $F$  while negative at  $L$ ), making the surface states along  $\bar{\Gamma} - \bar{M}$  robust and visible on any arbitrary crystal termination. However, given that  $\bar{K}$  is not a TRIM, the surface state along  $\bar{M} - \bar{K}$  cannot be protected solely by TRS. In this case the crystal symmetry adds another constraint. In the slab calculation, the full symmetry of the slab at the  $\bar{K}$  point is  $D_3$ . This double group has three different irreducible representations. Two of them have a  $C_3$  eigenvalue of  $-1$  and mirror eigenvalues of  $+/-i$ , which map to spin and are not constrained to be degenerate due to the non-TRIM nature of the  $\bar{K}$  point. The other irreducible representation has a  $C_3$  eigenvalue of  $+1$  and a mirror eigenvalue of  $0$ , and is doubly degenerate, regardless of the non-TRIM nature of the  $\bar{K}$  point. This implies that doubly degenerate states, from crystal symmetry, are possible even at the non-TRIM  $\bar{K}$  point, thus allowing for topologically protected states along the  $\bar{M} - \bar{K}$  direction. Due to the  $C_3$  symmetry at  $\bar{K}$ , some bands are doubly degenerate. This would have the result of pinning the states into doublets at the  $\bar{K}$  point, thus making the surface state along  $\bar{M} - \bar{K}$  protected by both TRS and  $C_3$  symmetries. Breaking either of these symmetries would result in a trivial surface state along the  $\bar{M} \rightarrow \bar{K}$  direction. It is worth noting, however, that breaking  $C_3$  symmetry would preserve the surface states along  $\bar{\Gamma} - \bar{M}$  as that is protected solely by TRS.

ARPES measurements were employed to experimentally probe the electronic structure of Cu-Zr<sub>2</sub>Te<sub>2</sub>P. The ARPES

intensity mappings along different directions denoted in Fig. 3(c) [Fig. 3(c) is an ARPES mapping of the Fermi surface] are shown in Figs. 3(d)–3(f). The high quality of the Cu-Zr<sub>2</sub>Te<sub>2</sub>P crystals employed is manifested in the sharp ARPES spectra. The third Dirac cone predicted by the DFT calculations is clearly observed [Fig. 3(e)] with a large energy window (over 2 eV) of linear dispersions around it. Its Dirac point is observed at the  $\bar{M}$  point at around  $-1.0$  eV, which agrees closely with the calculation. The cuts along the  $\bar{\Gamma} \rightarrow \bar{M}$  and  $\bar{\Gamma} \rightarrow \bar{K}$  directions [Figs. 3(d) and 3(f)] also match with the slab calculation. For instance, the cutoff energy ( $E_F$ ) measured in the intensity mapping along the  $\bar{\Gamma} \rightarrow \bar{K}$  direction is at the top of a highly dispersive band, confirming the calculation along the same direction. Also, along the  $\bar{\Gamma} \rightarrow \bar{M}$  direction, the bands are more dispersive near  $\bar{\Gamma}$  while becoming flat when close to  $\bar{M}$ . Both features are manifested in Fig. 3(d) taken along the same direction.

Despite the exotic Dirac features both inside the pseudogap above  $E_F$  and at around  $-1.0$  eV below  $E_F$ , the electronic properties of bulk Zr<sub>2</sub>Te<sub>2</sub>P are dominated by the electronic dispersions near  $E_F$ . In Fig. 2(a), the dispersive band stretching from the close proximity of the  $\Gamma$  point along the  $\Gamma - F$  and  $\Gamma - L$  directions suggests the existence of a dominant electron pocket at  $E_F$ . In addition, close to the  $\Gamma$  point, several bands cross  $E_F$  and form circular holelike Fermi surfaces. These two kinds of Fermi surface are clearly observed in the calculated bulk Fermi surface in Fig. 4(a), which is viewed down the  $\Gamma - Z$  direction. Due to the three-fold rotational and inversion symmetries of the compound, there are six ellipsoidal electron pockets around  $\Gamma$ . These electron pockets in fact host the Dirac cones at the  $\bar{M}$  points. The hole pockets centered at the  $\Gamma$  point are also displayed in Fig. 4(a), in different colors from the electron pockets.

The experimental Fermi surface obtained from the ARPES characterization is shown in Fig. 4(b). It shows the electron and hole pockets that are predicted by the DFT calculation. The dotted lines in the image outline the surface Brillouin zone. The plum-pit-shaped electron pockets along  $\bar{\Gamma} \rightarrow \bar{M}$  suggest that the surface-projected electronic structure is highly anisotropic. Figure 4(c) shows a stack of equal-energy-spaced constant-energy ARPES contours. The topmost map is at  $E_F$  while the bottom one is at  $-1.1$  eV from  $E_F$ . The white lines are drawn as a guide to the eye. The electron pocket narrows as the binding energy increases. The pocket shrinks linearly along the transverse direction ( $\bar{M} \rightarrow \bar{K}$ ) and vanishes at  $\bar{M}$  point, which corresponds to the Dirac point. Along the longitudinal direction ( $\bar{\Gamma} \rightarrow \bar{M}$ ), however, the pocket first shrinks linearly but more drastically when close to the Dirac point. This is consistent with the dispersion along  $\bar{\Gamma} \rightarrow \bar{M}$  [Fig. 3(d)] which is quite linear immediately down to  $E_F$  while it flattens out in the close proximity of the Dirac point.

*In situ* deposition in the ARPES chamber of a small amount of potassium on the surface of Zr<sub>2</sub>Te<sub>2</sub>P was employed to electron-dope the system so that normally unoccupied bands could be observed. With the bulk electronic structure almost intact, the potassium deposition we performed simply shifts the  $E_F$  upward by around 100–200 meV. Although the amount of doping was insufficient to observe the Dirac surface states predicted to exist inside the pseudogap, it revealed a new Dirac feature near  $E_F$  [Fig. 4(e)]. [The  $E_F$  in Figs. 4(d) and 4(e)

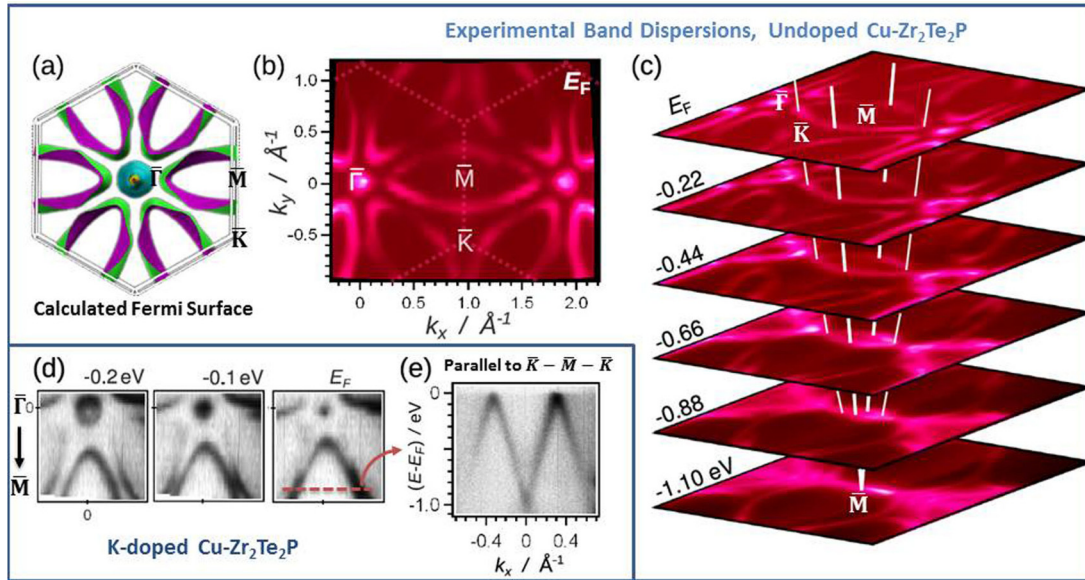


FIG. 4. (a) DFT-calculated Fermi surface viewed down the  $\Gamma - Z$  direction in the first Brillouin zone. (b) Intensity mapping of the experimental Fermi surface obtained from ARPES. The dotted lines in the image outline the boundaries of the surface Brillouin zone. (c) A stack of experimentally determined equal-energy-spaced constant-energy ARPES contours. The white lines are drawn as a guide to the eye. (d) The petal-like electron pockets were made to touch by electron doping of the bands. Constant-energy cuts show the shift of the band structure by some 150 meV. The red dotted line denotes where the electron pockets begin to touch. An energy-dependent mapping along this direction (parallel to  $\bar{M} \rightarrow \bar{K}$ ) is shown in (e).

represents the Fermi energy of  $n$ -doped  $\text{Cu-Zr}_2\text{Te}_2\text{P}$ , not the  $E_F$  of the pristine compound in Figs. 4(b) and 4(c)]. From  $-0.2$  eV to  $E_F$ , the electron pockets begin to touch each other at a point on the  $\bar{\Gamma} - \bar{K}$  azimuth. Here, the red dotted line in Fig. 4(d) points to an azimuth that is parallel to the  $\bar{M} \rightarrow \bar{K}$  direction. The energy-dependent mapping along this direction is shown in Fig. 4(e). Two Dirac nodes are observed close to the new  $E_F$ . Since the two Dirac nodes are away from TRIM points and are not protected by any crystalline symmetry, spin-orbit coupling results in gapped Dirac points. We deduce that these massive Dirac nodes come from the slightly gapped bulk-derived Dirac dispersion inside the pseudogap [Fig. S1(right)]. The Dirac nodes are positioned at 0.6 eV above the pristine  $E_F$  between  $M$  and  $K$  but lower in energy when traveling away from  $M-K$  towards  $\Gamma$ , leading to a Dirac node near the new  $E_F$  [shown in Fig. 4(e)]. Another Dirac-like crossing at around  $-1.0$  eV between the two massive Dirac nodes in Fig. 4(e) corresponds to the extension of the Dirac point along  $\bar{\Gamma} \rightarrow \bar{M}$ . This crossing is not gapless due to the tiny splitting of the dispersion along  $\bar{\Gamma} \rightarrow \bar{M}$  from the Dirac point. These bands therefore also connect to the surface states centered around  $\bar{M}$  as discussed earlier.

#### IV. CONCLUSION

In conclusion, we have reported the discovery of a strong topological metal,  $\text{Zr}_2\text{Te}_2\text{P}$ , where the band inversions are of the  $d$ - $p$  type.  $\text{Zr}_2\text{Te}_2\text{P}$  adopts the same crystal structure as the topological insulator  $\text{Bi}_2\text{Te}_2\text{Se}$ . It has two TRS-protected surface Dirac cones and one gapped 3D Dirac cone in its electronic structure. The Dirac cone at the  $\bar{\Gamma}$  point exists in a pseudogap at around 0.4 eV above  $E_F$ , which is a result

of the band inversion between  $\text{Zr } 4d$  orbitals and  $\text{Te } 5p$  orbitals. A second Dirac cone at the  $\bar{M}$  point is derived from an electron pocket at  $E_F$ , which shrinks when the energy is lowered and vanishes to a doubly degenerate Dirac point at  $-1.0$  eV. This Dirac cone is unusually anisotropic, with a linear dispersion along  $\bar{M} \rightarrow \bar{K}$  but an almost flat, nearly degenerate dispersion along  $\bar{\Gamma} \rightarrow \bar{M}$ , similar in some ways to the surface states observed in  $\text{Ru}_2\text{Sn}_3$  [24], the nature of which is still not understood. Unfortunately, the physical properties due to the second Dirac cone are unlikely to be isolated due to the coexistence of bulk bands in the same energy range. Nevertheless, this is apparently the first system to realize a TRS-protected Dirac cone at the  $\bar{M}$  point although that was predicted for the (111) surface of the Bi-Sb alloy system [25]. When  $E_F$  is shifted upward through electron doping, the Dirac pockets touch each other on the  $\bar{\Gamma} - \bar{K}$  azimuth, forming a massive Dirac node gapped by spin-orbit coupling. We propose that if  $E_F$  can be shifted into the pseudogap, it is possible to realize high electron mobility and strong anisotropy in this system. Both chemical doping and gating are promising methods to realize this goal.

#### ACKNOWLEDGMENTS

The authors thank Lukas Muehler, Liang-Yan Hsu and Bin Liu for helpful discussions. This work was supported by the ARO MURI on topological insulators, Grant No. W911NF-12-1-0461. The ARPES measurements at the Advanced Light Source were supported by the U.S. Department of Energy under Contracts No. DE-AC02-05CH11231 and No. DE-SC0012704.

- [1] T. Wehling, A. M. Black-Schaffer, and A. V. Balatsky, *Adv. Phys.* **63**, 1 (2014).
- [2] T. Liang, Q. Gibson, M. N. Ali, M. Liu, R. Cava, and N. Ong, *Nat. Mater.* **14**, 280 (2015).
- [3] J. Xiong, S. K. Kushwaha, T. Liang, J. W. Krizan, M. Hirschberger, W. Wang, R. Cava, and N. Ong, *Science* **350**, 413 (2015).
- [4] Y. Chen *et al.*, *Science* **325**, 178 (2009).
- [5] H. Zhang, C.-X. Liu, X.-L. Qi, X. Dai, Z. Fang, and S.-C. Zhang, *Nat. Phys.* **5**, 438 (2009).
- [6] L. Fu, C. L. Kane, and E. J. Mele, *Phys. Rev. Lett.* **98**, 106803 (2007).
- [7] L. Fu and C. L. Kane, *Phys. Rev. B* **76**, 045302 (2007).
- [8] S. M. Young, S. Zaheer, J. C. Y. Teo, C. L. Kane, E. J. Mele, and A. M. Rappe, *Phys. Rev. Lett.* **108**, 140405 (2012).
- [9] M. Neupane *et al.*, *Nat. Commun.* **5**, 3786 (2014).
- [10] Z. Liu *et al.*, *Nat. Mater.* **13**, 677 (2014).
- [11] Z. Liu *et al.*, *Science* **343**, 864 (2014).
- [12] Z. Ren, A. A. Taskin, S. Sasaki, K. Segawa, and Y. Ando, *Phys. Rev. B* **82**, 241306 (2010).
- [13] H. Ji, J. M. Allred, M. K. Fuccillo, M. E. Charles, M. Neupane, L. A. Wray, M. Z. Hasan, and R. J. Cava, *Phys. Rev. B* **85**, 201103 (2012).
- [14] K. Tschulik, M. Ruck, M. Binnewies, E. Milke, S. Hoffmann, W. Schnelle, B. P. T. Fokwa, M. Gilleßen, and P. Schmidt, *Eur. J. Inorg. Chem.* **2009**, 3102 (2009).
- [15] A. F. Kusmartseva, B. Sipoš, H. Berger, L. Forró, and E. Tutiš, *Phys. Rev. Lett.* **103**, 236401 (2009).
- [16] Y. S. Hor, A. J. Williams, J. G. Checkelsky, P. Roushan, J. Seo, Q. Xu, H. W. Zandbergen, A. Yazdani, N. P. Ong, and R. J. Cava, *Phys. Rev. Lett.* **104**, 057001 (2010).
- [17] See Supplemental Material at <http://link.aps.org/supplemental/10.1103/PhysRevB.93.045315> for Table I, which contains the structural characterization of Cu-Zr<sub>2</sub>Te<sub>2</sub>P, as well as Figs. S1 and S2, which are the band structures of Zr<sub>2</sub>Te<sub>2</sub>P in a hexagonal Brillouin zone and the DOS of Zr<sub>2</sub>Te<sub>2</sub>P, respectively.
- [18] D. J. Singh and L. Nordstrom, *Planewaves, Pseudopotentials, and the LAPW Method* (Springer Science & Business Media, New York, 2006).
- [19] G. K. H. Madsen, P. Blaha, K. Schwarz, E. Sjöstedt, and L. Nordström, *Phys. Rev. B* **64**, 195134 (2001).
- [20] E. Sjöstedt, L. Nordström, and D. Singh, *Solid State Commun.* **114**, 15 (2000).
- [21] J. Bland and S. Basinski, *Can. J. Phys.* **39**, 1040 (1961).
- [22] M. Yang and W.-M. Liu, *Sci. Rep.* **4**, 5131 (2014).
- [23] A. P. Weber, Q. D. Gibson, H. Ji, A. N. Caruso, A. V. Fedorov, R. J. Cava, and T. Valla, *Phys. Rev. Lett.* **114**, 256401 (2015).
- [24] Q. Gibson, D. Evtushinsky, A. N. Yarensko, V. B. Zabolotnyy, Mazhar N. Ali, M. K. Fuccillo, J. Van den Brink, B. Büchner, R. J. Cava, and S. V. Borisenko, *Sci. Rep.* **4**, 5168 (2014).
- [25] J. C. Y. Teo, L. Fu, and C. L. Kane, *Phys. Rev. B* **78**, 045426 (2008).